Applied Physics Letters

Brillouin zone center phonon modes in $ZnGa_2O_4$

Cite as: Appl. Phys. Lett. **117**, 052104 (2020); https://doi.org/10.1063/5.0012526
Submitted: 02 May 2020 . Accepted: 21 July 2020 . Published Online: 06 August 2020

Megan Stokey, Rafał Korlacki, Sean Knight, Matthew Hilfiker, Zbigniew Galazka, Klaus Irmscher, Vanya Darakchieva, and Mathias Schubert

Applied Physics Letters ARTICLE scitation.org/journal/apl

Brillouin zone center phonon modes in $ZnGa_2O_4$

Cite as: Appl. Phys. Lett. **117**, 052104 (2020); doi: 10.1063/5.0012526
Submitted: 2 May 2020 · Accepted: 21 July 2020 ·
Published Online: 6 August 2020

Megan Stokey,[1,a)] Rafał Korlacki,[1] Sean Knight,[1] Matthew Hilfiker,[1] Zbigniew Galazka,[2] Klaus Irmscher,[2] Vanya Darakchieva,[3] and Mathias Schubert[1,3,4]

AFFILIATIONS

[1]Department of Electrical and Computer Engineering, University of Nebraska-Lincoln, Lincoln, Nebraska 68588, USA
[2]Leibniz-Institut für Kristallzüchtung, 12489 Berlin, Germany
[3]Terahertz Materials Analysis Center and Center for III-N Technology, C3NiT–Janzèn, Department of Physics, Chemistry and Biology (IFM), Linköping University, 58183 Linköping, Sweden
[4]Leibniz Institut für Polymerforschung e.V., 01069 Dresden, Germany

[a)]**Author to whom correspondence should be addressed:** mstokey@huskers.unl.edu. **URL:** http://ellipsometry.unl.edu

ABSTRACT

Infrared-active lattice mode properties of melt-grown high-quality single bulk crystals of $ZnGa_2O_4$ are investigated by combined spectroscopic ellipsometry and density functional theory computation analysis. The normal spinel structure crystals are measured by spectroscopic ellipsometry at room temperature in the range of 100 cm^{-1}–1200 cm^{-1}. The complex-valued dielectric function is determined from a wavenumber-by-wavenumber approach, which is then analyzed by the four-parameter semi-quantum model dielectric function approach augmented by impurity mode contributions. We determine four infrared-active transverse and longitudinal optical mode pairs, five localized impurity mode pairs, and the high frequency dielectric constant. All four infrared-active transverse and longitudinal optical mode pairs are in excellent agreement with results from our density functional theory computations. With the Lyddane–Sachs–Teller relationship, we determine the static dielectric constant, which agrees well with electrical capacitance measurements performed on similarly grown samples. We also provide calculated parameters for all Raman-active and for all silent modes and, thereby, provide a complete set of all symmetry predicted Brillouin zone center modes.

Transparent conductive oxides have been the focus of much research effort due to their wide range of physical properties, which make them suitable, for example, for a large variety of electronic and optoelectronic device applications.[1–3] Divalent metal (Me)-based ternary Ga-based spinels, $MeGa_2O_4$, have recently regained interest due to their potential for growth in high-quality single-crystal phases and due to their potential for useful ultrawide bandgap semiconductor properties.[4,5] $ZnGa_2O_4$ (zinc gallate; ZGO) is one of such materials with a bandgap energy of 4.59 ± 0.03 eV, assuming a direct optical transition (or of about 4.3 eV assuming an indirect optical transition) reported recently by Galazka *et al.*[4] The ultrawide bandgap semiconductor β-Ga_2O_3 (gallium sesquioxide) has similar large bandgap energy values, which strongly depend on the polarization direction within the highly anisotropic crystal structure.[4,6,7] This monoclinic symmetry phase of gallium oxide is a contemporary material of interest with high promise for use in high-power, high-voltage applications.[8–11] Where β-Ga_2O_3 continues to be a difficult material to work with due to its crystallographic monoclinic symmetry, $ZnGa_2O_4$ offers a promising high-symmetry alternative. Galazka *et al.* recently demonstrated controllable electrical conductivity in bulk $ZnGa_2O_4$ single crystals including highly electrically insulating material.[4] For example, a Hall mobility of about 100 $cm^2/V\,s$ at a free electron concentration of approximately 1×10^{19} cm^{-3} was reported. Such a high Hall mobility for such a large free electron concentration is currently unavailable in single crystal substrates of β-Ga_2O_3. Good electrical mobility at a high carrier concentration can make bulk single crystal ZGO suitable for applications in future vertical configuration high-power high-voltage devices.[12]

At present, very little is known about fundamental physical properties of ZGO. Transition metal ion-doped ZGO has been reported as long-lasting high brightness phosphor for *in vivo* imaging using x-ray phosphorescence and thermally stimulated luminescence.[13] Chemical and thermal stabilities make it suitable for use in plasma and field emission devices.[14] Yang *et al.* reported synthesis of ZGO as multimetallic mesoporous materials with improved photocatalytic activity for CO_2 reduction.[15] While ZGO has been grown and researched as a single crystal grown from flux[16–18] since the late 1960s, most previously published work focused on thin films, ceramics, and polycrystalline

samples.[13,19–22] Phonon modes are of basic interest for understanding carrier and heat transport or photoexcitation processes, for example. While some information on infrared (IR)-active as well as Raman-active modes was reported, a complete set of IR-active transverse (TO) and longitudinal optical (LO) phonon modes in ZGO is not available yet.[23–27] Preudhomme and Tarte[28] provided an early IR study of vibrational modes in II–III spinels. López *et al.*[27] and López-Moreno *et al.*[29] reported Raman-active modes, IR-active TO modes, and silent modes from density functional theory (DFT) calculations. López *et al.*[27] and Van Gorkom *et al.*[24] reported experimental Raman scattering results without identifying all Raman-active modes. In this work, we provide calculated parameters for all Brillouin zone center phonon modes from DFT calculations, and we report the IR-active TO and LO phonon modes, obtained from spectroscopic ellipsometry analysis, in melt-grown high-quality bulk single crystal ZGO. We find all predicted IR-active modes in excellent agreement with our DFT calculations, and we report on the observation of additional, potentially impurity-related modes.

ZGO single crystals were obtained directly from the melt by the vertical gradient freeze method (VGF), as described in detail by Galazka *et al.*[4] The obtained crystals were sliced with surfaces of (100) and (111) orientations, annealed at 1100 °C in air for 10 h, cut into wafers of $10 \times 10 \times 0.5$ mm^3, lapped, and one-side polished. As reported in Ref. 4, the sample growth conditions lead to electrically insulating crystals by annealing in the presence of oxygen at temperatures ≤ 700 °C for at least several hours. Hence, our samples were colorless and electrically insulating. Samples were measured as received without further treatment. Radio frequency (RF) capacitance measurements (test frequency 1 kHz…1 MHz; test level 100 mV) were performed in a capacitor geometry with 7 mm diameter gold contacts electron-beam evaporated on a ZGO wafer polished on both sides.

ZGO crystallizes in the cubic spinel structure (space group 227, F-3dm, Fig. 1). There are 14 atoms (2 chemical units) in the primitive cell, which produce 42 phonon modes, of which three with T_{1u} symmetry are acoustic modes and the Γ-point optical modes are classified as follows:

$$\Gamma_{\mathrm{opt}} = A_{1g} + 2A_{2u} + 2E_u + E_g + 4T_{1u} + 2T_{2u} + T_{1g} + 3T_{2g}.$$

All T-symmetry modes are triple-degenerate, and E-symmetry modes are double degenerate, for a total of 39 optical modes at the Brillouin zone center. A_{1g}, E_g, and T_{2g} modes are Raman-active. The IR-active modes T_{1u} split into TO and LO modes. All other modes are silent.

Spectroscopic ellipsometry is a contact-less measurement technique, which measures the change in polarization of light ($\tilde{\rho}$) caused by interaction with the sample. In reflection ellipsometry, this change can be written as

$$\tilde{\rho} = \frac{\tilde{r}_p}{\tilde{r}_s} = \tan(\Psi) e^{i\Delta}, \quad (1)$$

where $\tilde{r}_p$ and $\tilde{r}_s$ are the Fresnel reflection coefficients for the light polarized parallel to (p) and perpendicular (s) to the plane of incidence. The rotation of the light's polarization state about the axis of propagation is defined as Ψ, and the relative phase shift between the parallel and perpendicular components is defined as Δ. Hence, for each wavenumber, a (Ψ, Δ) pair is measured.

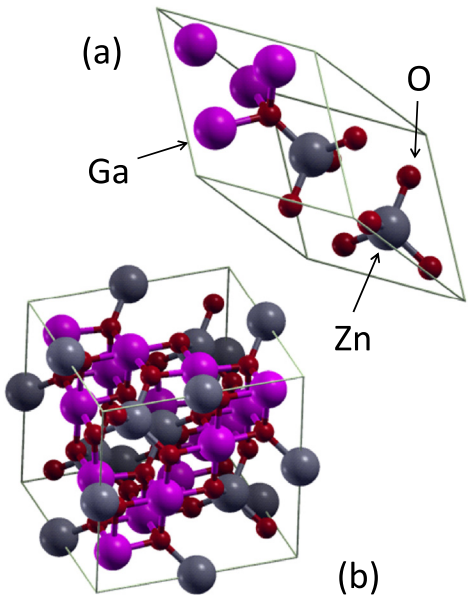

FIG. 1. Primitive (a) and conventional (b) cells of the spinel structure ZGO crystal. Note that both cells have the same orientation with respect to an external coordinate system.

Two instruments were used to obtain the ellipsometric data. Mid-infrared data were taken from 500 cm^{-1}–1200 cm^{-1} using a commercially available variable angle of incidence spectroscopic ellipsometer (IR-VASE Mark-II; J.A. Woollam Co., Inc.). Far-infrared ellipsometry was performed from 100 cm^{-1}–500 cm^{-1} using an in-house built FIR-VASE ellipsometer.[30] Data were acquired at angles of incidence of $\Phi_a = 50°$ and 70°. Measurements were repeated at multiple sample azimuths and found to be identical as expected due to the isotropic optical properties of the cubic spinel structure. Measurements were performed on two different samples, one of each with (100) and (111) surface orientations, respectively. All measurements were performed in stable, ambient conditions at room temperature. During analysis, data from both samples were combined and analyzed simultaneously. We note that datasets from different samples are identical to within the noise. Analysis was performed using WVASE 32™ (J.A. Woollam Co., Inc.). Experimental data are shown in Fig. 2. We use the half-infinite ambient-substrate approximation for model analysis. No surface roughness is considered because the samples are highly polished, and residual nanometer-scale roughness does not contribute to the ellipsometric data in the mid-infrared and far-infrared regions.[31] We first analyze the experimental data using a wavenumber-by-wavenumber best-match model calculation searching for the values of the real and imaginary parts of the substrate dielectric function. In this process, all parameters, the wavenumber-dependent dielectric function values, are searched for independently, i.e., without any specific model line shape assumption. The resulting best-match model-calculated ellipsometry data are shown in Fig. 2. Then, the wavenumber-by-wavenumber obtained dielectric function was analyzed using the so-called four-parameter semi-quantum (FPSQ) model first described by Gervais and Periou.[32] This model permits direct access to TO and LO mode frequencies, $\omega_{\mathrm{TO},l}$ and $\omega_{\mathrm{LO},l}$, and allows

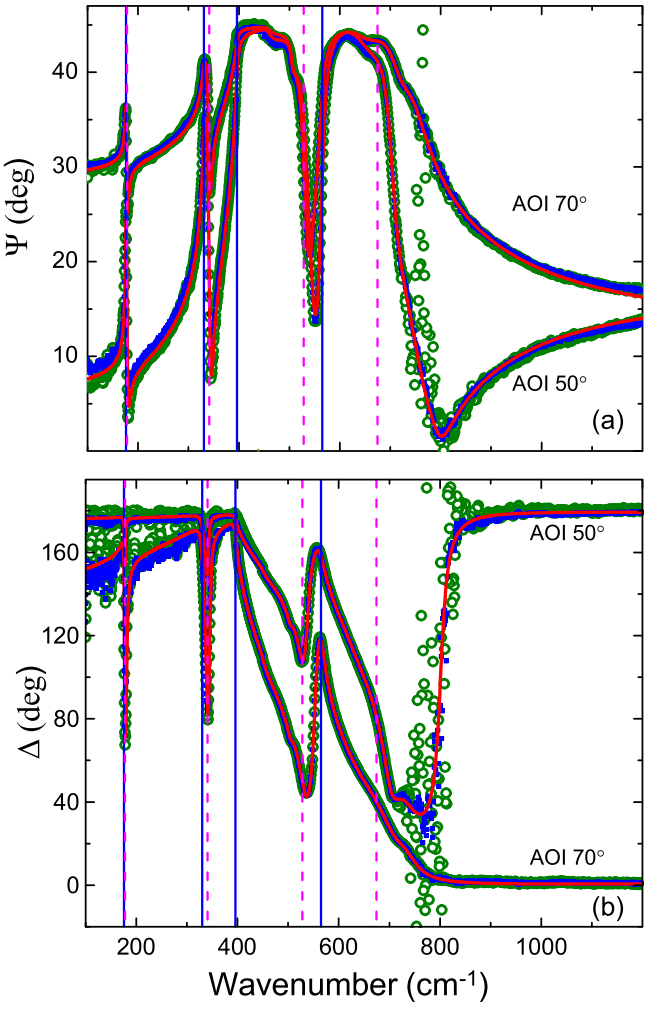

FIG. 2. Experimental (green open symbols), wavenumber-by-wavenumber best-match model (blue closed symbols) and best-match dielectric function model (red solid line) calculated Ψ (a) and Δ (b). Vertical blue solid lines indicate TO modes, magenta dashed lines indicate LO modes, and gold dotted lines indicate impurity modes identified in this work.

for determination of their independent broadening parameters, $\gamma_{\mathrm{TO},l}$ and $\gamma_{\mathrm{LO},l}$, respectively,

$$\varepsilon = \varepsilon_\infty \prod_{l=1}^{N+M} \frac{\omega_{\mathrm{LO},l}^2 - \omega^2 - i\omega\gamma_{\mathrm{LO},l}}{\omega_{\mathrm{TO},l}^2 - \omega^2 - i\omega\gamma_{\mathrm{TO},l}}, \tag{2}$$

where ε_∞ is the high-frequency dielectric constant.[31] The product runs over all $N=4$ phonons (TO–LO pairs) with T_{1u} symmetry. In addition, as will be discussed further below, we identify $M=5$ impurity modes (I-1, …, I-5) with small polarity, i.e., with $\omega_{\mathrm{LO},l}^2 - \omega_{\mathrm{TO},l}^2 \approx 0$.[33,34] The Lyddane–Sachs–Teller (LST) relation[35] then permits the calculation of the static dielectric constant, $\varepsilon_{\mathrm{DC}}$,

$$\frac{\varepsilon_{\mathrm{DC}}}{\varepsilon_\infty} = \prod_{l=1}^{N+M} \frac{\omega_{\mathrm{LO},l}^2}{\omega_{\mathrm{TO},l}^2}, \tag{3}$$

using all other parameters in Eq. (2) determined from analysis of the wavenumber-by-wavenumber obtained ε.

Theoretical calculations were performed using plane wave DFT code Quantum ESPRESSO (QE).[36] We used the local density approximation exchange-correlation functional of Perdew and Wang (PW)[37,38] and optimized norm-conserving Vanderbilt (ONCV) scalar-relativistic pseudopotentials.[39] As the starting point, we used structural parameters from the Materials Project.[40,41] The initial structure was first relaxed to force levels less than 10^{-6} Ry Bohr^{-1}. A regular shifted $4 \times 4 \times 4$ Monkhorst–Pack grid was used for sampling of the Brillouin zone.[42] A convergence threshold of 1×10^{-12} Ry was used to reach selfconsistency with a large electronic wavefunction cutoff of 200 Ry. The relaxed cell was used for subsequent phonon calculations. The phonon frequencies, Born effective charges, IR intensities, and Raman scattering activities[43] were computed at the Γ-point of the Brillouin zone using density functional perturbation theory,[44] as implemented in the Quantum ESPRESSO package, with the convergence threshold for self-consistency of 1×10^{-18} Ry. The parameters of the TO modes were obtained from the dynamical matrix computed at the Γ-point. The parameters of the LO modes were obtained by setting a small displacement from the Γ-point in order to include the long-range Coulomb interactions of Born effective charges in the dynamical matrix (the so-called non-analytical terms). We note that DFT calculations were performed disregarding effects of finite temperature.

Our DFT analysis results are summarized in Table I for all IR-active and all Raman modes and in Fig. 5 for all silent modes. Renderings of the eigenvectors (the atomic displacement patterns, normalized to an arbitrary magnitude in order to visualize together modes with diverse oscillator strengths), prepared using XCrysDen[45] running

TABLE I. Parameters for IR-active and Raman-active phonon modes obtained from DFT calculations in this work and compared with literature data where available. Frequencies, ω_{TO} and ω_{LO}, and IR intensities, A_{TO}^2 and A_{LO}^2, respectively, of TO and LO modes are presented for IR-active modes. Frequencies, ω_{RA}, and Raman scattering activities, S_{RA}, are provided for Raman-active modes. Frequencies for silent modes are shown in Fig. 5. Values of ε_∞ and $\varepsilon_{\mathrm{DC}}$ are determined to be 4.128 and 10.63, respectively, using the LST relationship.

Mode	ω_{TO} (cm^{-1})	ω_{TO} (cm^{-1})	ω_{LO} (cm^{-1})	A_{TO}^2 $[\frac{(\mathrm{D/\AA})^2}{\mathrm{amu}}]$	A_{LO}^2 $[\frac{(\mathrm{D/\AA})^2}{\mathrm{amu}}]$
T_{1u}-1	561.36	580[a]	663.97	9.046	58.309
T_{1u}-2	396.18	429[a]	521.71	50.534	8.208
T_{1u}-3	332.18	342[a]	338.81	6.714	0.200
T_{1u}-4	174.00	175[a]	175.54	0.481	0.057
	ω_{RA} (cm^{-1})	ω_{RA} (cm^{-1})	ω_{RA} (cm^{-1})	ω_{RA} (cm^{-1})	S_{RA} (Å^4/amu)
A_{1g}	705.88	717[a]	714[b]	706[c]	50.77
E_g	368.66	395[a]	…[b]	…[c]	0.0651
T_{2g}-1	600.89	618[a]	611[b]	606[c]	4.784
T_{2g}-2	468.21	488[a]	467[b]	462[c]	0.5469
T_{2g}-3	183.43	186[a]	…[b]	…[c]	0.0115

[a]Theory (DFT), Refs. 27 and 29.
[b]Exp. (Raman), Ref. 23.
[c]Exp. (Raman), Ref. 27.

under Silicon Graphics Irix 6.5, are presented in Fig. 3 (IR-active modes), Fig. 4 (Raman-active modes), and Fig. 5 (silent modes). Note the diversity of the participating constituents and the complexity of their respective displacement pattern for all modes, where a simple subdivision into vibrations within or among sub-blocks within the spinel structure cannot be upheld. Our results for the IR-active TO mode frequencies as well as for the Raman-active and silent modes are consistent with the DFT-calculated phonon modes frequencies reported by López *et al.*[27] and López-Moreno *et al.*[29] (Table I). Calculated LO modes have not been reported yet, and neither were the intensities of the IR-active modes or activities of the Raman-active modes. The latter are very small for the E_g and T_{2g}-3 modes, which may explain why these were not detected in the experiments in Refs. 24 and 27.

Our spectroscopic ellipsometry analysis identified four IR-active TO–LO mode pairs as predicted by DFT. These modes, all with T_{1u} symmetry, can be clearly seen in the dielectric function, which is shown in Fig. 6. The best-match model dielectric function parameters are listed in Table II. The TO mode frequencies are mostly in agreement with those reported by Van Gorkom *et al.*[24] and Preudhomme and Tarte[28] also listed in Table II. LO mode frequencies were not reported from experiment so far. Our mode frequency parameters

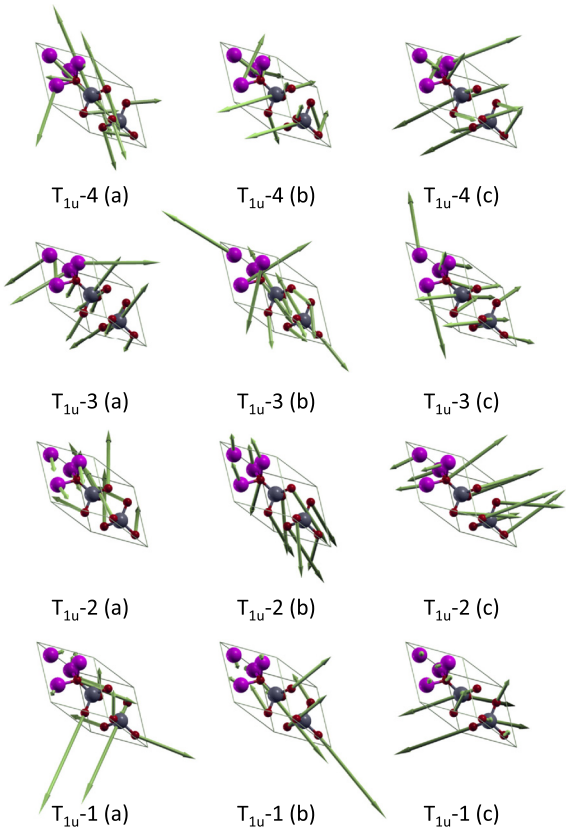

FIG. 3. Atomic displacement eigenvectors for IR-active phonon modes in the spinel structure single bulk crystal of ZGO. Because T_{1u} modes are triple-degenerate, three eigenvectors labeled (a)–(c) are shown for each phonon mode. Note that the transition dipoles are orthogonal to each other for all triplets. Color scheme: gray—Zn, purple—Ga, and red—O.

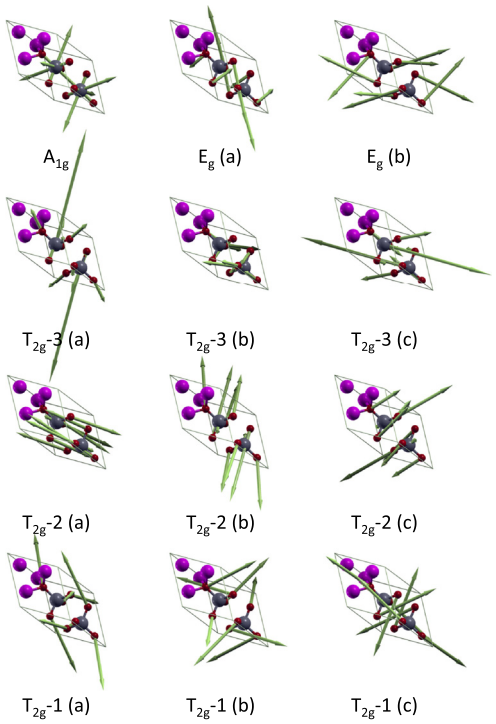

FIG. 4. Atomic displacement eigenvectors for Raman-active phonon modes in the spinel structure single bulk crystal of ZGO. Because E_g modes are double-degenerate and T_{1u} modes are triple-degenerate, two, and three eigenvectors, respectively, labeled (a)–(c), are shown for these modes.

determined from experiment are slightly shifted up in wavenumber with respect to our findings from DFT calculations; however, the agreement is still considered excellent. Additionally, contributions due to impurity modes similar to those previously described by Kasic *et al.*[33] for single-crystalline GaN and Schöche *et al.*[34] for TiO_2 were detected in our experimental data. We report five such modes. Their contributions to the dielectric function are best seen in Fig. 7, where we depict the same data shown in Fig. 6 but on a logarithmic scale for the imaginary parts of ε and its inverse, ε^{-1}. We note that the peaks within the former identify TO modes, while within the latter identify LO modes. This can be clearly observed in Figs. 6(a) and 6(b), respectively, and labeled accordingly. Impurity modes appear as peaks with much smaller amplitude and with frequency identical between the two spectra shown. This can be observed by contributions identified with vertical green dotted lines, labeled accordingly. We note that none of the observed impurity modes fall within the vicinity of our DFT derived Raman-active or silent modes, and their origins cannot be ruled out as being due to elemental impurities or structural defects. At present, the exact origins are unknown. We note an increase in noise toward the lower as well as toward the higher wavenumber region in Fig. 7, which is due to the fact that the samples become transparent outside the phonon mode regions. In regions where a sample is transparent, the intensity of light reflected from the samples reduces and thereby increases the error bars on our ellipsometry data. This can be verified with the increase in noise in the same spectral regions in Fig. 2. However, this uncertainty affects the accuracy little within

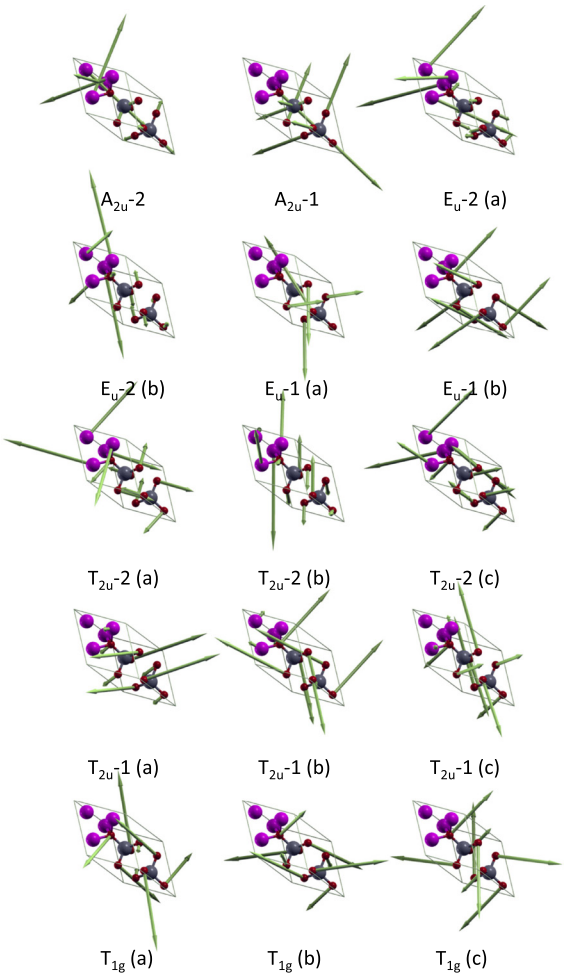

FIG. 5. Atomic displacement eigenvectors for silent phonon modes in the spinel structure single bulk crystal of ZGO. DFT-calculated frequencies of these modes are (numbers in brackets from Refs. 27 and 29) 403.20 (419) cm^{-1} (A_{2u}-2), 694.57 (702) cm^{-1} (A_{2u}-1), 218.65 (229) cm^{-1} (E_u-2), 547.04 (563) cm^{-1} (E_u-1), 130.14 (135) cm^{-1} (T_{2u}-2), 422.09 (450) cm^{-1} (T_{2u}-1), and 335.56 (366) cm^{-1} (T_{1g}). Because E_u modes are double-degenerate and T_{2u} and T_{1g} modes are triple-degenerate, two and three eigenvectors, respectively, labeled (a)–(c), are shown for these modes.

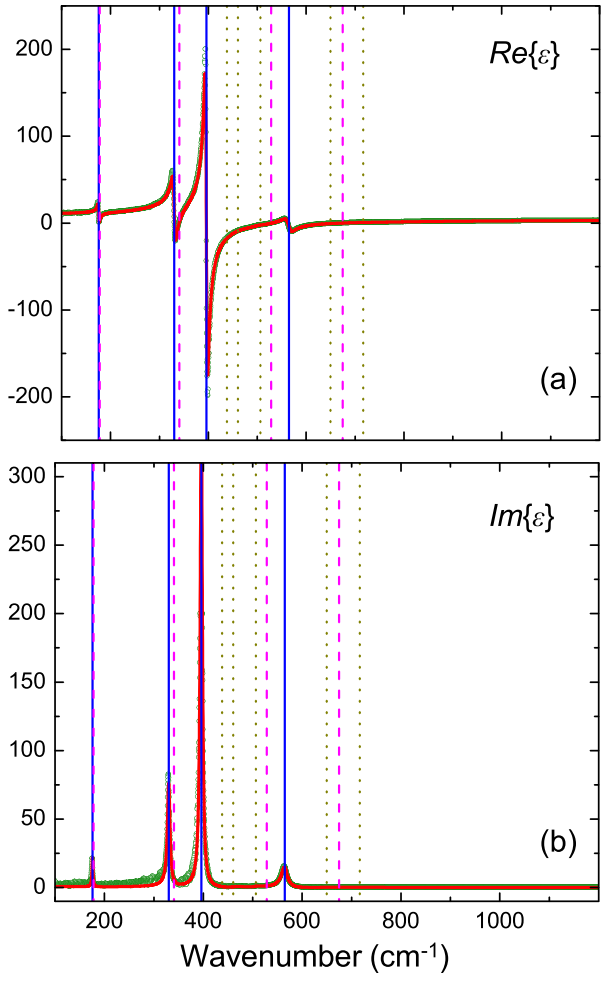

FIG. 6. Wavenumber-by-wavenumber best-match model calculated (green open symbols) and best-match model dielectric function calculated (red solid line) real (a) and imaginary (b) parts of the dielectric function. Vertical blue solid lines indicate TO modes, magenta dashed lines indicate LO modes, and gold dotted lines indicate impurity modes identified in this work.

which the phonon and impurity modes can be determined across the phonon mode spectral region.

In Table II, ε_∞ was obtained as a best-match mode dielectric function parameter to be 3.78 ± 0.02, and a ε_{DC} value of 10.5 ± 0.06 was then obtained using the LST relation. RF capacitance measurements enabled us to directly determine the static dielectric constant for a similar, insulating sample and resulted in a ε_{DC} value of 11.3 ± 0.7. This value is slightly higher than ε_{DC} extrapolated using the LST relationship and consistent within uncertainty limits with the DFT value. We note that both values are almost in agreement within uncertainty limits, while yet unaccounted for possible defect-activated resonances at longer wavelengths would further raise the extrapolated value using the LST relationship. The LST relationship provides the ratio between ε_{DC} and ε_∞, which is a measure for the amount of charge displacement stored within the optical phonons of a polar lattice. We find this ratio similar for spinel ZGO and for β-Ga_2O_3 when for the latter, anisotropic values are averaged over the monoclinic crystal directions.[46] Also, ε_{DC} are similar between the two compounds. Hence, one can anticipate for ZGO intrinsic free charge mobility limitations by phonon scattering at room temperature comparable to those in β-Ga_2O_3.[47] Thus, in addition to the attractiveness of ZGO due to its isotropic lattice structure, we suggest that ZGO could be a suitable candidate for high power device materials.

In summary, we have measured mid-infrared and far-infrared spectroscopic ellipsometry parameters on melt-grown high-quality single bulk crystals of ZGO. We obtained the complex-valued dielectric function first from a wavenumber-by-wavenumber data inversion approach and then by matching a four-parameter semi-quantum model dielectric function model. We observe all four symmetry

TABLE II. FPSQ model parameters for TO, LO, and impurity modes obtained from best-match model dielectric function analysis. ε_∞ and ε_{DC} are determined to be 3.78 ± 0.02, and 10.5 ± 0.06 using the LST relationship.

Mode	ω_{TO} (cm^{-1})	ω_{TO} (cm^{-1})	ω_{TO} (cm^{-1})	ω_{LO} (cm^{-1})	γ_{TO} (cm^{-1})	γ_{LO} (cm^{-1})
T_{1u}-1	564.83 ± 0.08	570[a]	593[b]	674.6 ± 2.6	14.9 ± 0.16	5.3 ± 1.6
T_{1u}-2	395.99 ± 0.04	420[a]	455[b]	528.2 ± 0.45	5.28 ± 0.06	16.3 ± 0.42
T_{1u}-3	330.10 ± 0.04	328[a]	333[b]	340.68 ± 0.05	6.37 ± 0.08	4.98 ± 0.07
T_{1u}-4	175.83 ± 0.03	175[a]	175[b]	177.94 ± 0.04	2.29 ± 0.06	2.36 ± 0.06
I-1	716 ± 8.5			726 ± 10	76 ± 17.2	76 ± 13.8
I-2	649 ± 11.3			648 ± 12.0	81 ± 19.5	66 ± 18.7
I-3	506 ± 1.2			505 ± 1.5	13 ± 2.4	11 ± 2.1
I-4	460.2 ± 0.87			460.3 ± 0.8	27 ± 3.0	26 ± 2.8
I-5	438[c]			439[c]	36[c]	37[c]

[a]Exp. (IR absorption), Ref. 23.
[b]Exp. (IR absorption), Ref. 28.
[c]Parameter manually held in fit.

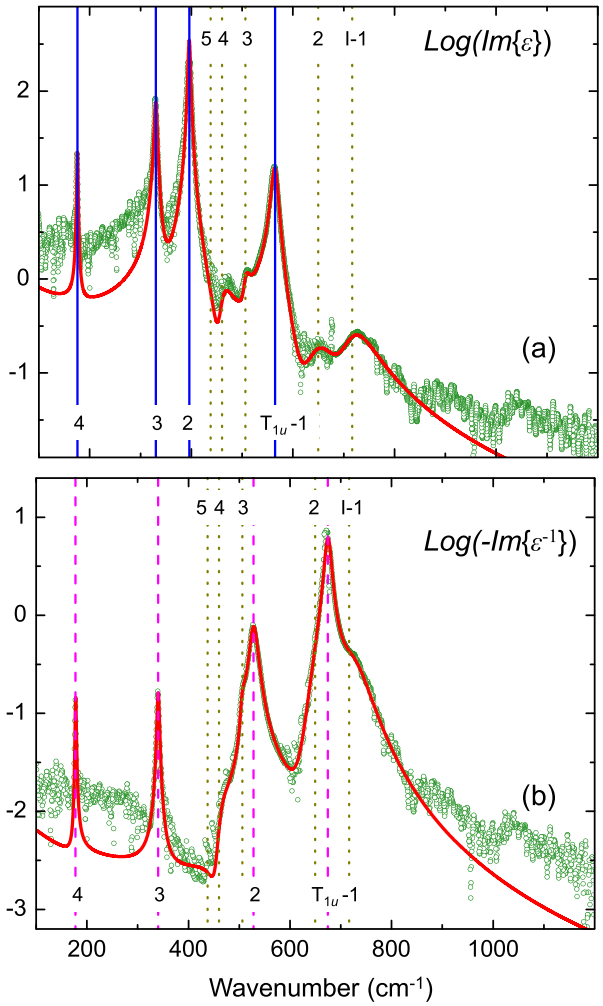

FIG. 7. The same data and line styles as shown in Fig. 6, where (a) shows the imaginary part of ε and (b) shows the imaginary part of its inverse. Note the logarithmic scales for the ordinates.

predicted IR-active lattice modes, split into TO and LO mode pairs. All four IR-active TO and LO modes are in excellent agreement with results from our DFT computations. With the LST relationship, we determine the static and high frequency dielectric constants. We further identify five impurity mode pair contributions, whose physical origin remains unknown so far. We provide all Brillouin zone center Raman and silent mode parameters. Our results are comparable with incomplete sets of mode parameters obtained previously from polycrystalline samples and DFT studies.

This work was supported in part by the National Science Foundation under Award No. DMR 1808715, the Air Force Office of Scientific Research under Award No. FA9550-18-1-0360, the Nebraska Materials Research Science and Engineering Center under Award No. DMR 1420645, the Swedish Research Council VR under Award No. 2016-00889, the Swedish Foundation for Strategic Research under Grant Nos. RIF14-055 and EM16-0024, the Swedish Governmental Agency for Innovation Systems VINNOVA under Competence Center Program Grant No. 2016-05190, the Knut and Alice Wallenbergs Foundation supported grant "wide-bandgap semiconductors for next generation quantum components," and the Swedish Government Strategic Research Area in Materials Science on Functional Materials at Linköping University, Faculty Grant SFO Mat LiU No. 2009-00971. Megan Stokey acknowledges the University of Nebraska Foundation and the J. A. Woollam Foundation for financial support.

DATA AVAILABILITY

The data that support the findings of this study are available from the corresponding author upon reasonable request.

REFERENCES

[1]M. Grundmann, H. Frenzel, A. Lajn, M. Lorenz, F. Schein, and H. von Wenckstern, Phys. Status Solidi A **207**, 1437 (2010).
[2]M. Lorenz, M. S. R. Rao, T. Venkatesan, E. Fortunato, P. Barquinha, R. Branquinho, D. Salgueiro, R. Martins, E. Carlos, A. Liu, F. K. Shan, M. Grundmann, H. Boschker, J. Mukherjee, M. Priyadarshini, N. DasGupta, D. J. Rogers, F. H. Teherani, E. V. Sandana, P. Bove, K. Rietwyk, A. Zaban, A. Veziridis, A. Weidenkaff, M. Muralidhar, M. Murakami, S. Abel, J.

Fompeyrine, J. Zuniga-Perez, R. Ramesh, N. A. Spaldin, S. Ostanin, V. Borisov, I. Mertig, V. Lazenka, G. Srinivasan, W. Prellier, M. Uchida, M. Kawasaki, R. Pentcheva, P. Gegenwart, F. M. Granozio, J. Fontcuberta, and N. Pryds, J. Phys. D: Appl. Phys. **49**, 433001 (2016).
[3]S. J. Pearton, J. Yang, P. H. Cary, F. Ren, J. Kim, M. J. Tadjer, and M. A. Mastro, Appl. Phys. Rev. **5**, 011301 (2018).
[4]Z. Galazka, S. Ganschow, R. Schewski, K. Irmscher, D. Klimm, A. Kwasniewski, M. Pietsch, A. Fiedler, I. Schulze-Jonack, M. Albrecht, T. Schröder, and M. Bickermann, APL Mater. **7**, 022512 (2019).
[5]Z. Galazka, D. Klimm, K. Irmscher, R. Uecker, M. Pietsch, R. Bertram, M. Naumann, M. Albrecht, A. Kwasniewski, R. Schewski, and M. Bickermann, Phys. Status Solidi A **212**, 1455 (2015).
[6]A. Mock, R. Korlacki, C. Briley, V. Darakchieva, B. Monemar, Y. Kumagai, K. Goto, M. Higashiwaki, and M. Schubert, Phys. Rev. B **96**, 245205 (2017).
[7]Z. Galazka, Semicond. Sci. Technol. **33**, 113001 (2018).
[8]M. Higashiwaki, K. Sasaki, A. Kuramata, T. Masui, and S. Yamakoshi, Phys. Status Solidi A **211**, 21 (2014).
[9]M. Higashiwaki and G. H. Jessen, Appl. Phys. Lett. **112**, 060401 (2018).
[10]Z. Xia, H. Chandrasekar, W. Moore, C. Wang, A. J. Lee, J. McGlone, N. K. Kalarickal, A. Arehart, S. Ringel, F. Yang, and S. Rajan, Appl. Phys. Lett. **115**, 252104 (2019).
[11]J. Zhang, J. Shi, D.-C. Qi, L. Chen, and K. H. L. Zhang, APL Mater. **8**, 020906 (2020).
[12]T. J. Flack, B. N. Pushpakaran, and S. B. Bayne, J. Electron. Mater. **45**, 2673 (2016).
[13]A. Bessière, S. Jacquart, K. Priolkar, A. Lecointre, B. Viana, and D. Gourier, Opt. Express **19**, 10131 (2011).
[14]I. J. Hsieh, K. T. Chu, C. F. Yu, and M. S. Feng, J. Appl. Phys. **76**, 3735 (1994).
[15]S. Yan, S. Ouyang, J. Gao, M. Yang, J. Feng, X. Fan, L. Wan, Z. Li, J. Ye, Y. Zhou, and Z. Zou, Angew. Chem., Int. Ed. **49**, 6400 (2010).
[16]Z. Yan and H. Takei, J. Cryst. Growth **171**, 131 (1997).
[17]P. J. Van der Straten, R. Metselaar, and H. D. Jonker, J. Cryst. Growth **43**, 270 (1978).
[18]A. B. Chase and J. A. Osmer, J. Am. Ceram. Soc. **50**, 325 (1967).
[19]S. H. Tsai, S. Basu, C. Y. Huang, L. C. Hsu, Y. G. Lin, and R. H. Horng, Sci. Rep. **8**, 14056 (2018).
[20]S. K. Sampath, D. G. Kanhere, and R. Pandey, J. Phys.: Condens. Matter **11**, 3635 (1999).
[21]W. K. Wang, K. F. Liu, P. C. Tsai, Y. J. Xu, and S. Y. Huang, Coatings **9**, 859 (2019).
[22]W. K. Wang, Y. J. Xu, S. Y. Huang, K. F. Liu, and P. C. Tsai, Coatings **9**, 469 (2019).
[23]G. G. Van Gorkom, J. H. Haanstra, and H. v. d. Boom, J. Raman Spectrosc. **1**, 513 (1973).
[24]G. G. Van Gorkom, J. C. Henning, and R. P. Van Stapele, Phys. Rev. B **8**, 955 (1973).
[25]J. E. Drake and J. Simpson, Spectrochim. Acta, Part A **24**, 981 (1968).
[26]H. A. Lauwers and M. A. Herman, J. Phys. Chem. Solids **41**, 223 (1980).
[27]S. López, A. H. Romero, P. Rodríguez-Hernández, and A. Muñoz, Phys. Rev. B **79**, 214103 (2009).
[28]J. Preudhomme and P. Tarte, Spectrochim. Acta, Part A **27**, 1817 (1971).
[29]S. López-Moreno, P. Rodríguez-Hernández, A. Muñoz, A. H. Romero, F. J. Manjón, D. Errandonea, E. Rusu, and V. V. Ursaki, Ann. Phys. **523**, 157 (2011).
[30]P. Kühne, C. M. Herzinger, M. Schubert, J. A. Woollam, and T. Hofmann, Rev. Sci. Instrum. **85**, 071301 (2014).
[31]M. Schubert, *Infrared Ellipsometry on Semiconductor Layer Structures: Phonons, Plasmons and Polaritons*, Springer Tracts in Modern Physics Vol. 209 (Springer, Berlin, 2004).
[32]F. Gervais and B. Piriou, J. Phys. C **7**, 2374 (1974).
[33]A. Kasic, M. Schubert, S. Einfeldt, D. Hommel, and T. E. Tiwald, Phys. Rev. B **62**, 7365 (2000).
[34]S. Schöche, T. Hofmann, R. Korlacki, T. E. Tiwald, and M. Schubert, J. Appl. Phys. **113**, 164102 (2013).
[35]R. H. Lyddane, R. Sachs, and E. Teller, Phys. Rev. **59**, 673 (1941).
[36]Quantum ESPRESSO is available from http://www.quantum-espresso.org. See also: P. Giannozzi, S. Baroni, N. Bonini, M. Calandra, R. Car, C. Cavazzoni, D. Ceresoli, G. L. Chiarotti, M. Cococcioni, I. Dabo, A. D. Corso, S. de Gironcoli, S. Fabris, G. Fratesi, R. Gebauer, U. Gerstmann, C. Gougoussis, A. Kokalj, M. Lazzeri, L. Martin-Samos, N. Marzari, F. Mauri, R. Mazzarello, S. Paolini, A. Pasquarello, L. Paulatto, C. Sbraccia, S. Scandolo, G. Sclauzero, A. P. Seitsonen, A. Smogunov, P. Umari, and R. M. Wentzcovitch, J. Phys.: Condens. Matter **21**, 395502 (2009).
[37]J. P. Perdew and Y. Wang, Phys. Rev. B **45**, 13244 (1992).
[38]J. P. Perdew and Y. Wang, Phys. Rev. B **98**, 079904 (2018).
[39]M. J. van Setten, M. Giantomassi, E. Bousquet, M. J. Verstraete, D. R. Hamann, X. Gonze, and G. M. Rignanese, Comput. Phys. Commun. **226**, 39 (2018).
[40]A. Jain, S. P. Ong, G. Hautier, W. Chen, W. D. Richards, S. Dacek, S. Cholia, D. Gunter, D. Skinner, G. Ceder, and K. A. Persson, APL Mater. **1**, 011002 (2013).
[41]K. Persson, "Materials Data on $Zn(GaO_2)_2$ (SG:227) by Materials Project" (United States, 2014).
[42]H. J. Monkhorst and J. D. Pack, Phys. Rev. B **13**, 5188 (1976).
[43]P. L. Polavarapu, J. Phys. Chem. **94**, 8106 (1990).
[44]S. Baroni, S. de Gironcoli, A. D. Corso, S. Baroni, S. de Gironcoli, and P. Giannozzi, Rev. Mod. Phys. **73**, 515 (2001).
[45]A. Kokalj, J. Mol. Graphics Modell. **17**, 176 (1999). Code available from http://www.xcrysden.org.
[46]M. Schubert, R. Korlacki, S. Knight, T. Hofmann, S. Schöche, V. Darakchieva, E. Janzén, B. Monemar, D. Gogova, Q.-T. Thieu, R. Togashi, H. Murakami, Y. Kumagai, K. Goto, A. Kuramata, S. Yamakoshi, and M. Higashiwaki, Phys. Rev. B **93**, 125209 (2016).
[47]N. Ma, N. Tanen, A. Verma, Z. Guo, T. Luo, H. G. Xing, and D. Jena, Appl. Phys. Lett. **109**, 212101 (2016).